Optical probing of hot expanded states produced by shock release

P. Celliers and A. Ng
Department of Physics, Univerisity of British Columbia, British Columbia, Vancouver, Canada V6T 1Z1
(Received 16 June 1992; revised manuscript received 2 November 1992)

The angle and polarization dependence of optical emission and reflection from dense aluminum plasmas produced in the release wave of a strong shock is investigated theoretically. It is shown that with high-speed measurements (few-picosecond resolution), optical probing of the unloading plasma can be used to examine transport properties and ionization balance of thermodynamic states in the vicinity of the liquid-vapor critical point. The calculations were performed using data from two wide-ranging theoretical models of plasma conductivity, a semianalytical model due to Lee and More [Phys. Fluids **27**, 1273 (1984)] and a partial-wave analysis due to Rinker [Phys. Rev. B **31**, 4207 (1985); **31**, 4220 (1985)]. The models predict substantially different values for the conductivity close to the liquid-vapor critical point (more than a factor of 10 for the electron-ion collison time); the different results obtained for the two models sugest that experimental measurements could provide new information for improving the current understanding of dense plasma properties.

PACS number(s): 52.35.Tc, 52.25.Rv

I. INTRODUCTION

The properties of dense plasmas have been under intense study in recent years. Experimental studies on dense plasmas are usually limited to localized regions of the density-temperature plane. The regimes accessible by various experimental methods in the case of aluminum are shown in Fig. 1. At low temperatures, relatively complete equation-of-state data, including measurements of electrical conductivity, and sound speed have been made using the isobaric expansion technique pioneered by Gathers and co-workers [1,2]. This method appears to be limited to maximum pressures of a few kbar, and expansions to about 50% larger than the normal volume. An important method for obtaining dense plasma states with high thermal energy density is with shock-release experiments. Impedance-match experiments have been used to determine the release isentropes of metals such as Cu, Pb, Bi, and Al [3–5]. Another promising approach for accessing the ultrahigh-pressure regime uses laser-driven shocks [6–9]. Studies of luminous emission [10] and rear-surface reflectivity [11] show potential for yielding information on temperatures and transport properties in the unloading plasma. A more recent experimental development has been the use of femtosecond (fs) laser pulses to heat a solid metallic surface to temperatures of several eV in a time short enough that the surface does not expand appreciably [12]. The reflected light signal contains information that leads to the determination of the material temperature as well as the resistivity. Since the material remains condensed on this time scale, the technique has the potential to yield nearly isochoric data.

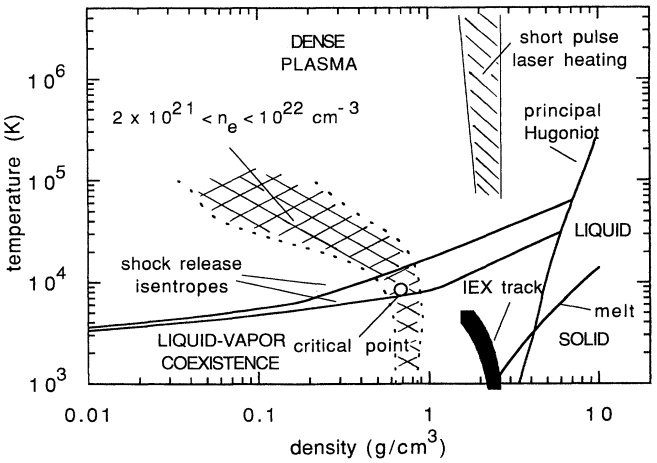

FIG. 1. Density-temperature sketch for aluminum showing areas relevant to this study. Labeled on the diagram are the principal Hugoniot curve, the melting curve, and the trajectory of a 3-kbar isobar (IEX track) measured in Ref. [2]. Also shown are two shock-release isentropes computed with the QEOS equation of state, and the critical point (also computed with QEOS). The cross-hatched area bounded by the dotted curves identifies regions where the electron densities yield plasma frequencies equal to visible optical frequencies. The hatched area bounded by solid curves identifies regions accessible to high-intensity short-pulse laser experimentation.

In this paper we investigate the shock-release problem in detail and examine the utility of optical probing using emission and reflectivity measurements. The aim of the paper is to show that (i) such measurements can provide detailed and complementary information on the electrical conductivity within a relatively small range of densities and temperatures in the unloading plasma, and that (ii) an experimental temperature determination of the emitting plasma layer at early times after the shock breakout (10–100 ps) ought to be possible in spite of a large theoretical uncertainty in the plasma conductivity. The results of our calculations show that very different brightness temperatures and reflectivities are predicted, depending on the conductivity model used in the calculations. (The reflectivity calculations are summarized by Fig. 11, and brightness temperatures by the open symbols

in Fig. 14.) Brightness temperature measurements alone would be inaccurate as a means of temperature determination, especially for early times in the shock release, because the emissivity is unaccounted for, and a theoretical estimate for the emissivity is evidently unreliable. However, by correcting the brightness temperature using results from a reflectivity measurement one could obtain quite good agreement with the true temperature of the emitting region—which is an important objective of the measurements. This correction produces accurate results independently of the conductivity model used in the calculations. Thus the two measurements taken together could be used to provide a temperature determination which is independent of any calculation. This type of correction is possible because both emission and reflection take place within the same plasma layer, as we show in this paper. Taken individually, the reflectivity of the plasma depends on the electrical conductivity in the reflecting layer [11], while the emission (i.e., brightness temperature) depends on both the temperature and the emissivity in the emitting layer. Since both processes take place in the same layer, knowledge of the true temperature in this layer makes comparison of both types of measurements with calculations far more valuable. Finally, we show how a spectrally resolved measurement of the Doppler shift in a reflected probe beam may be used to infer (with some theoretical input) the density and ionization state of the emitting and/or reflecting plasma layer.

The advantage of shock-produced plasmas is that they are readily generated by a number of methods including explosively accelerated flyers, gas-gun accelerated flyers, laser ablation, and nuclear explosions. Such shock states are reproducible and can be well characterized. For the strong shocks investigated in this study the most viable method of producing the state is with laser-driven ablation [6–9]. The shock release is produced by propagating a strong shock (typically >5 Mbar for aluminum) through a solid target so that it reaches a vacuum interface on the rear side. The pressure release of the hot, shocked-compressed material results in a backward propagating rarefaction wave, and a plasma or vapor cloud expanding into the vacuum. States in the release wave have temperatures ranging from <1 eV up to a few eV and densities ranging from zero up to the compressed solid densities in the shocked material. The plasma states in this region are hot enough to produce significant visible emission. Furthermore, the conductivity is high enough to produce a reflecting, critical density surface in the expanding profile, where the plasma frequency matches the optical probe frequency. The cross-hatched region in Fig. 1 shows the region of electron densities (2×10^{21}–10^{22} cm^{-3}) with plasma frequencies corresponding to frequencies in the optical range of the visible spectrum (wavelength range: 350–700 nm). For the purposes of identifying this region we have used an average ionization state calculation by Rinker [13]. The intersection of this band of electron densities with the liquid-vapor coexistence boundary also coincides with the approximate location in density-temperature space where a metal-insulator transition may be expected to occur. Evidently, with careful choice of initial conditions and probe frequency it may be possible to probe near the liquid-vapor critical point. Initial experiments observing both the luminous emission and reflectivity from such a shock-released plasma have already demonstrated the basic experimental techniques [10,11,14,15].

The shock-release problem was previously surveyed by Zel'dovich and Raizer [16,17] over 30 years ago. At that time diagnostic methods achieved only nanosecond resolutions. For this relatively long time scale, optical emission and absorption in the shock-released plasma is dominated by a cool, optically thick layer of metallic vapor consisting of neutral and singly ionized atoms, which is formed at the low-density tail of the release wave. With modern high-speed instrumentation (up to picosecond resolution) it becomes possible to probe denser regions of the shock release, where the optical depth at optical frequencies is limited mainly to the skin depth of the steep density profile in the release wave at early times after release. Only at later times (nanoseconds) has the profile expanded so much that a cool layer of low-density vapor obscures the high-density high-temperature regions behind.

If an optical measurement can be performed within about 100 ps of the shock release, the cool screening layer is insufficiently developed to hinder probing of the dense regions behind it. The emission or reflection of optical radiation will then originate *primarily* from a localized region of the expanding profile near the critical density layer corresponding to the given probe frequency, and suffer negligible absorption in the lower density regions. The density of this localized region depends on the ionization state of the sample material along the release isentrope, and on the probe frequency. Precise theoretical or experimental determinations of the ionization state are not yet available. In general the ionization state is expected to vary rapidly with density in the vicinity of the liquid-vapor critical point.

Picosecond time resolution is still insufficient to observe optical radiation originating or reflecting from the shocked material at the highest (Hugoniot) densities. This is because the critical density layer, which is cooler and of lower density than the shock state, also acts as a reflecting layer to radiation passing through it in either direction. Accurate optical characterization of the Hugoniot state for an initially opaque metallic sample requires at lease subpicosecond time resolution to allow data collection before the critical density layer expands a few optical depths away from the hot, shock-compressed material.

In examining the reflectivity and luminous emissions for aluminum shocked to 10 Mbar, we have performed calculations based on solutions of electromagnetic wave propagation in an inhomogeneous plasma profile. One of the aims of the study is to compare two different wide-ranging models for plasma conductivity, a semianalytic model by Lee and More [18], and a partial-wave calculation due to Rinker [13]. We also show how both the angle and polarization dependence of the reflectivity and emission may be utilized to provide information on plasma conductivity, temperature, and ionization state.

II. SHOCK-RELEASED STATES

Arrival of a strong shock at a free surface (vacuum interface) leads to a backward traveling rarefaction wave in which the material reaches states of reduced density and temperature. When thermal transport processes (electron conduction or radiation transport) are insignificant the release process is adiabatic, and the states attained in the release wave lie along the isentrope passing through the initial shock state. We consider an initial state on the Hugoniot curve brought about by the arrival of a strong shock traveling in the positive z direction at the rear surface of a target at position $z=0$, and time $t=0$. If the equation of state of the material is known, then the release wave can be described parametrically through the following expressions [17]:

$$\frac{z}{t}=u(\rho)-c_s(\rho)\ , \tag{1}$$

$$u(\rho)=u_0-\int_{\rho_0}^{\rho}c_s(\rho')\frac{d\rho'}{\rho'}\ . \tag{2}$$

The initial density ρ_0 and particle speed u_0 are those on the Hugoniot curve, and the particle velocity u and all the thermodynamic quantities in the expanding density profile are functions of a self-similar coordinate, z/t. The density and temperature profiles in time and space can be obtained from an integral which follows a path down the isentrope leading from the initial state. The integrand contains the isentropic sound speed $c_s(\rho)$ along the isentrope. The sound speed and all the thermodynamic parameters such as pressure and temperature must be obtained from an appropriate equation of state. Integral expressions relating two states on a given isentrope are easily obtained using the second law of thermodynamics and the equation of state. It is evident that accurate knowledge of the material equation of state (EOS) along the entire isentrope is essential for producing accurate release profiles. Moreover, theoretical models of material properties such as conductivities and ionization state are usually parametrized as functions of material density and temperature. This places further importance on accurate calculations of the density and temperature profiles in the release wave.

A. Equation-of-state models

Along the Hugoniot curve, the EOS for many materials is well known, both theoretically and experimentally. However, in the region of expanded states above the liquid-vapor critical point, which we investigate in this study, both theoretical and experimental information is scarce. For practical hydrodynamic calculations it is necessary to use a wide-ranging model which spans many decades on the density-temperature plane. To assess the accuracy of this approach we compare two currently available EOS models. One is an aluminum EOS available in the SESAME computer library of Los Alamos National Laboratory [19] and the other is based on the quotidian equation-of-state (QEOS) model of More *et al.* [20].

The SESAME EOS was generated as a combination of seven theoretical models which are expected to be accurate and valid in different regions of density-temperature space, and is described in Ref. [21]. Four of these models apply specifically to density-temperature regions relevant to the release isentropes examined in this study. In the compressed liquid region with densities near the Hugoniot curve ($\rho>4.0$ g/cm^3) the variational liquid metal pseudopotential method was used to compute the EOS [22]. At the opposite extreme, in the region of the low-density, high-temperature plasma ($\rho<0.1$ g/cm^3, $T>2$ eV) a nonideal plasma statistical expansion model due to Rogers [23] was used. At low densities and intermediate temperatures, where the material state is that of a partially ionized monatomic vapor, a Saha ionization balance model was applied [24]. Finally, in the low-temperature liquid-vapor coexistence region a soft sphere liquid structure model developed by Young [25] was used. This model contains several parameters which were adjusted to fit isobaric expansion data. It is important to note that these models are essentially independent as they are based on rather different physical pictures. Along the boundaries joining different models the equation of state may not be thermodynamically self-consistent. For example, various thermodynamic identities relating derivatives on the EOS surface may not hold in these regions. Furthermore, in the density-temperature range of $0.2<\rho<2.0$ g/cm^3 and $1<T<20$ eV, no appropriate model was available so that the EOS data were produced by an interpolation scheme to bridge the gap. It is interesting to note that this is also where the release isentropes pass just above the liquid-vapor critical point. As with any tabular model the SESAME EOS can produce noisy derivatives (such as the sound speed) on the EOS surface.

The QEOS model is based on a simpler scheme. It is almost analytic and is based on a wide-ranging free energy description from which all thermodynamic functions can be obtained in a thermodynamically self-consistent manner. It combines a Thomas-Fermi description [26] of the electron free energy with the Cowan model [20] for the ion free energy that includes an adequate description of the solid, liquid, and gas (plasma) phases. The Barnes correction [27] is used to match the cold curve to the known density and bulk modulus at normal solid conditions. The QEOS model produces accurate results in various limits or special cases (normal solid conditions, high-density limit, high-temperature limit, and low-density limit) while in the more complicated intermediate regimes its accuracy does not match that of the best available models. Specifically, in the region of low-temperature expanded states the QEOS model is not expected to be accurate. In this study we have used a slightly modified version of QEOS in which we have introduced an additional parameter, the cohesive energy, which provides a better description of the low-temperature region. For this we have modified the functional form of the Barnes correction at expanded densities such that it matches the bulk modulus at solid density and also produces the correct cohesive energy [28] (the Barnes correction does not do this, additional details are described in the appendix). This modification affects

mainly the liquid-vapor coexistence region and the location of the critical point. For compressed states the model uses the standard Barnes correction. In the region of expanded states below the liquid-vapor critical point the QEOS model produces van der Waals loops along the isotherms. These were eliminated using the Maxwell construction [29] to produce smooth isotherms and isentropes within the liquid-vapor coexistence region.

The location of the critical point predicted by our modified version of QEOS is at a temperature of $T_c = 8556$ K and density $\rho_c = 0.685$ g/cm^3. This compares favorably with a number of phenomenological predictions of the critical point of metals [30–32], which place the critical point for aluminum around $T_c = 7000$–8000 K and $\rho_c \sim 0.6$–0.7 g/cm^3. However, more recent isobaric expansion measurements due to Gathers and Ross [2] have been fitted with the soft sphere model due to Young [25] to yield a critical temperature of $T_c = 5726$ K. This value is significantly lower, and probably more accurate since it is based on a fit to experimental results. The SESAME EOS incorporates Young's soft sphere results and is therefore likely to be more realistic around and below the critical point.

Both the SESAME and QEOS models predict Hugoniot curves that agree with each other, and with experimental data to better than a few percent for the mechanical parameters (density, pressure, particle speed). Much larger disagreement is evident when temperatures are compared. To assess this disagreement we show a comparison of the Hugoniot curves, and a series of release isentropes on the density-temperature plane in Fig. 2. A series of shock pressures is indicated for the initial Hugoniot shock states. Temperatures along the Hugoniot curve and along the release isentropes for various shock pressures are seen to differ by as much as a factor of 2. The largest discrepancies occur on the low isentropes and at low densities. The agreement improves in the limit of ultrastrong shock strengths at high temperature and high density. However, even for the highest isentropes there is a significant difference in temperatures towards the low-density region. Temperature is the most uncertain thermodynamic parameter in equation-of-state theory. It is also a parameter which is difficult to measure for shock states, particularly in opaque materials.

Aside from the differences between the two models it is also evident from Fig. 2 that, in the case of aluminum, the shock strength must be larger than about 5 Mbar in order to reach isentropes that pass above the liquid-vapor critical point. For lower shock strengths the isentropes intersect the liquid branch of the coexistence region. The exact location of the coexistence region is not well known, and since it has considerable influence on the paths of isentropes that pass near or through it, we have restricted our study to a 10-Mbar shock in which the release isentrope lies above the critical point, and intersects the coexistence region only at very low densities. This makes both experimental interpretation and theoretical analysis simpler because it obviates the need for considering vapor condensation and the formation of a two phase flow when the release isentrope enters the coexistence region from the liquid branch. Alternatively, high isentropes can be attained by shocking porous materials at lower pressures, but this method is likely not viable for the high time-resolution measurements intended in this study. This is because temporal and spatial inhomogeneities introduced by the pore scale length are usually of the order of 1 μm or larger for metal powders, which is too large for thermal and mechanical equilibrium to be reached in the shock front on the 10–100-ps time scales considered here.

Figure 3 shows the release profiles obtained from two hydrodynamic simulations of the release of a 10-Mbar shock in aluminum (shock speed $u_{\text{shock}} = 24$ km/s). In each simulation the initial state was set to the Hugoniot state, with $\rho_0 = 7.1$ g/cm^3, $T_0 = 6.0 \times 10^4$ K, $P_0 = 10$ Mbar, and $u_0 = 15.1$ km/s. This represents the standard initial state for all the calculations discussed in this paper. Both simulations used the same thermal conductivi-

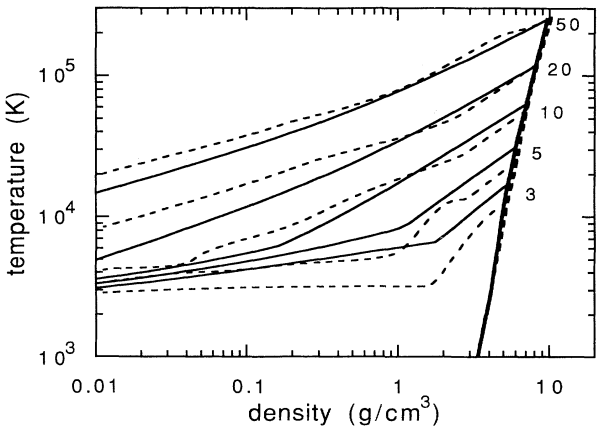

FIG. 2. Comparison of release isentropes calculated with the SESAME equation-of-state model (dashed) and QEOS model (solid). Release isentropes are centered on Hugoniot states with the shock pressures in Mbar indicated in the figure. The Hugoniot curves from both models are also shown.

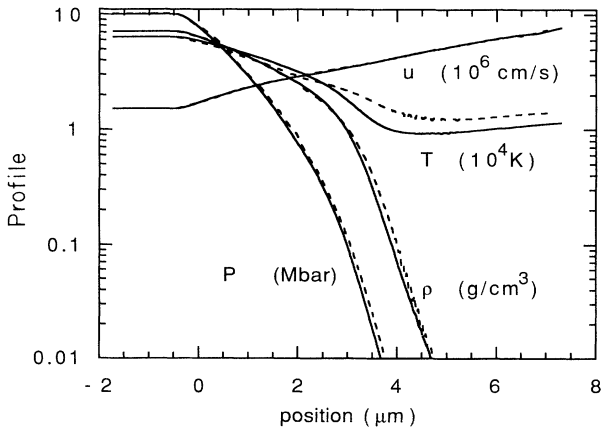

FIG. 3. Comparison of release profiles calculated using the SESAME (dashed) and QEOS (solid) models. Profiles of pressure P, density ρ, particle speed u, and temperature T, as a function of position are shown at $t = 100$ ps after the shock release. The position coordinate is fixed to the laboratory reference frame.

ty model, obtained from Rinker's transport calculations [13]. It should be noted that the profiles shown in this figure are not isentropic because of the inclusion of thermal conduction in the simulations; this will be discussed below. Two curves for each parameter are presented in the figure; the solid curve is from a simulation using the QEOS model, whereas the dashed curve is from one using the SESAME EOS. Remarkably the pressure, density, and particle speed profiles agree to within a few percent. The largest discrepancy is found in the predicted temperatures with differences amounting to as much as 30%. This is similar in magnitude to the discrepancies between the 10-Mbar isentropes on the density-temperature plane of Fig. 2. This close agreement is somewhat fortuitous, since the 10-Mbar isentropes appear to have the best agreement of all the curves shown in Fig. 2. Simulations at other shock conditions would not show as good agreement between the two EOS models.

In the absence of experimental or theoretical EOS data in the region above the liquid-vapor critical point, it is difficult to give an absolute assessment of the reliability of the calculated release profiles, since both the SESAME and QEOS models reduce to interpolations in this region. On the basis of the above comparisons we may conclude that the EOS descriptions available to us provide a remarkably consistent description of the mechanical parameters (P, ρ, and u) of the release density profile. Temperatures in the release wave appear to be less certain since this parameter is much more sensitive to the model used. The main effects of a variation in the temperature within the release wave will be to change the conductivity and also absolute emission levels. Absolute emission intensities (Planck intensities) in the visible wavelengths scale linearly with temperature above about 1 eV; however, the conductivity scales in a more complicated fashion that depends on the particular model. Along the release isentrope in the vicinity of the critical point, both the conductivity and the ionization state in the plasma have significant density dependences (according to the theoretical models discussed below), which are less problematical since the two EOS models predict very similar density profiles. We believe that the temperature uncertainties have a relatively small effect on the main conclusions of this study, although any temperature uncertainties will produce quantitative uncertainties that are important to consider when analyzing experimental data. With no overriding reason to favor one EOS model over the other, we have used the QEOS model as the basis for all of the calculations presented here since it is thermodynamically self-consistent, and has numerical qualities superior to the tabular SESAME model.

B. Conductivity and ionization models

In order to calculate the optical properties of the release wave, we require knowledge of electrical conductivity and ionization state. More specifically, the electron-ion collision frequency and ionization state are needed to construct a frequency-dependent dielectric function throughout the release profile based on the Drude model.

Two wide-ranging transport models for plasma conductivity were available. The first is a semianalytical model given by Lee and More [18]. The second is a partial-wave calculation by Rinker [13] which is available from Los Alamos National Laboratory as part of the SESAME materials properties database (material no. 23713).

The model due to Lee and More is based on an application of the Boltzmann transport equation in the relaxation time approximation, using Fermi-Dirac statistics to describe the electron momentum distribution. Relaxation times are computed including contributions from both electron-ion and electron-neutral scattering. For electron-ion scattering the standard Coulomb cross section is used in conjunction with various prescriptions for computing the Coulomb logarithm. These are developed to account for the physical effects of Debye-Hückel screening, strong coupling, and electron degeneracy. In strongly coupled plasmas, the Debye-Hückel screening length becomes less than the interatomic separation. This difficulty is avoided in the model by phenomenologically limiting the screening length to a minimum value equal to the interatomic separation. To agree with accurate partial-wave calculations in dense plasmas, the Coulomb logarithm is also limited to a value greater than 2. In the dense solid as well as the liquid metal regions where ion-ion correlations attain a much longer range, the Bloch-Grüneisen expression for metallic conductivity [33] is applied to compute the electron mean free path. Finally, there is a region in density-temperature space where the calculated electron mean free path is less than the mean distance between ions. In this region the mean free path is limited to a value equal to the ion sphere radius, and the relaxation time is then obtained from the mean electron speed. For aluminum this region is located in a density-temperature region approximately given by $0.6 < \rho < 1$ g/cm^3 and $2 < T < 20$ eV.

The conductivity model of Rinker is based on an application of the t-matrix formulation of the Ziman theory [34]. For these calculations Rinker adopts the average atom picture in which the electrons are scattered from a set of ion core potentials distributed statistically throughout the medium. In the interstitial regions the electrons are assumed to travel in plane-wave states, while the ion cores are assumed to be identical, nonoverlapping, and spherically symmetric. In this formulation four ingredients are required, namely, the ion structure factor, the electron-ion scattering cross section, the density of free electrons, and the electron chemical potential. The latter three quantities are computed self-consistently from the electron-ion potentials which are generated from a combination of various statistical mean-field models including the Thomas-Fermi-Dirac (TFD) statistical model (to generate the density and temperature dependence), the Hartree-Fock-Slater mean-field atomic model [35], and the temperature-dependent TFD-like model due to Liberman [36] (the latter two provide a low-density low-temperature limit). For the electron scattering cross section Rinker used a full partial-wave calculation. The ion structure factors were applied independently. The

calculations used various choices including the Debye-Hückel structure fact, the Perkus-Yevick liquid metal structure factor, and a third form which interpolates between the Debye-Hückel and the hard sphere limits. Rinker's application of Ziman theory depends on the assumption of single-site scattering. In strongly scattering systems this assumption is questionable and has been left as an open question.

The average ionization state is an important parameter in our Drude approximation of the plasma conductivity, because it determines the density range within the release profile where most of the absorption and emission takes place. In Rinker's model this parameter arises naturally out of the quantum-mechanical solutions obtained in computing the electronic structure. It is obtained essentially by finding the number of electrons occupying freely propagating states. Rinker defines the average ionization state to be the number of unbound electrons per atom occupying plane-wave states in the region between the ions. This definition treats any continuum electrons occupying resonance states as being effectively bound. Lee and More's conductivity model requires the ionization state, as well as the electron chemical potential, to be provided as input parameters to their model, which have to be calculated separately. The ionization state was computed with a screened hydrogenic model [37], and the chemical potential was computed with the Thomas-Fermi statistical atom model [26].

Both conductivity models provide data for the dc electrical conductivity σ_0, electron thermal conductivity, κ, and average ionization state Z as a function of density and temperature in a tabular format. To obtain the plasma dielectric function for the analysis discussed in the next section, a frequency-dependent Drude model is assumed for which the important parameters are the electron-ion collision time τ_{ei} and the electron plasma frequency ω_p. These are given by

$$\frac{1}{\tau_{ei}} = \frac{Zn_i e^2}{m\sigma_0} , \tag{3}$$

$$\omega_p^2 = \frac{4\pi Z n_i e^2}{m} , \tag{4}$$

where n_i is the ion density, m is the electron mass, and e is the electron charge. With these definitions, the frequency-dependent Drude expression for the conductivity is

$$\sigma(\omega) = \frac{\omega_p^2}{4\pi(1/\tau_{ei} - i\omega)} , \tag{5}$$

which is used to construct a frequency-dependent dielectric function.

We compare the data provided by the two conductivity models in Fig. 4 along the density-temperature path occurring at $t = 100$ ps after the shock release, as calculated with the hydrodynamic simulations. The figure displays curves of the ionization state Z and the electron-ion collision time τ_{ei}. In the dense ionized liquid

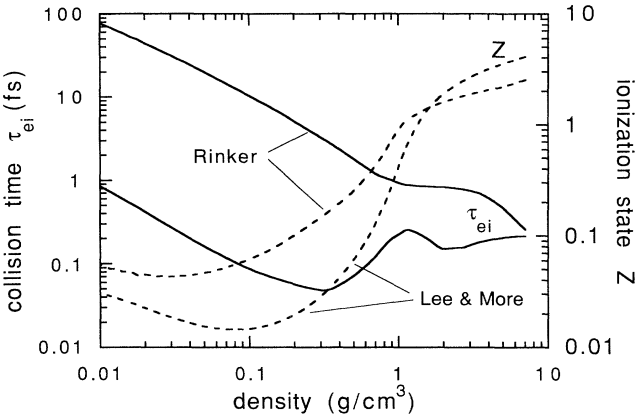

FIG. 4. Comparison of ionization state Z (dashed) and electron-ion collision time τ_{ei} (solid), as a function of density along the release profile at time $t = 100$ ps (see Fig. 3). Data from the conductivity models of Lee and More and Rinker are indicated in the figure.

the predicted ionization state is near the expected valence state of 3, although neither Rinker's nor Lee and More's model produces this value exactly. In the expanded region below 1 g/cm^3 both models predict quite different values for Z, especially at low temperatures. Any variation in the ionization state shifts the electron plasma frequency, and hence the location along the density profile of the reflection point for visible radiation where the plasma frequency equals the optical frequency.

Also of interest are the different predictions for the electron-ion collision rate especially in the low-density region. One may note that at optical frequencies the normalized collisionality is $\omega\tau_{ei} \simeq 1$ for τ_{ei} in the range $0.2 < \tau_{ei} < 0.4$ fs. In general we see that $\omega\tau_{ei} > 1$ for Rinker's model, and $\omega\tau_{ei} < 1$ for Lee and More's model. Furthermore, Lee and More's model predicts a collision time that is nearly two orders of magnitude smaller than that predicted by Rinker's model in the regime of expanded states with density less than 1 g/cm^3. The reason for the large difference in the collision time is not obvious. It may be connected with the approach to the neutral atom limit as the plasma recombines. Lee and More's model includes electron-neutral scattering explicitly, and it is an important scattering process at these densities. This effect is further magnified by the fact that the average ionization state in Lee and More's calculation is significantly lower in the expanded states. In Rinker's model scattering by neutral atoms is not explicitly included, since the model is based on the average atom picture. However, the approach to the neutral atom limit poses difficult problems at low temperatures [13]. Additionally the single-site scattering assumption may also be questionable in this range. It should be noted that both models were intended to describe dense ionized plasmas, and are in better agreement at higher temperature (and higher ionization states). The strong disagreement between both models suggests the need for improvement in current theoretical descriptions in the low-temperature, partially ionized region of the density-temperature plane.

C. Thermal transport

The analysis of shock-release states usually assumes an isentropic release path. However, at very early times after shock release the rarefaction wave is not isentropic. In fact, an isothermal release is more appropriate on very short time scales ($t < 1$ ps). This is because the thermal conductivity of the shocked state is large enough to enforce nearly isothermal conditions down the density gradient as the material begins to expand. Eventually, isothermal conditions give way to an isentropic expansion as the scale length of the rarefaction wave increases. A characteristic time scale during which this transition takes place is given by [38]

$$\tau_\kappa \sim 3.7 \frac{\kappa T}{\rho c_s^4} , \tag{6}$$

where κ is the thermal conductivity, T the temperature, ρ the density, and c_s the sound speed of the Hugoniot curve (initial state before release). The 10-Mbar shock state on the principal Hugoniot curve for aluminum gives a value of $\tau_\kappa \simeq 5$ ps. Although heat conduction becomes negligible for times larger than τ_κ, the temperature profile is sufficiently modified by the initial injection of heat that it is not described accurately by the isentrope until times $t \gg \tau_\kappa$.

Results of simulations which demonstrate this behavior are shown in Fig. 5. The isentrope leading from the initial state is shown as the dashed curve. States throughout the expanding profile at various times are shown as a series of curves which approach the isentrope with increasing time. One may note that, at early times, temperatures in the release wave dip slightly below the isentrope at the high-temperature high-density end, and are heated to values far above the isentrope at the cooler low-density end. This reflects the transfer of heat from the hotter high-density part of the release wave to the cooler expanding vapor. On time scales extending to about $t \sim 100$ ps after the shock release one observes a rapidly cooling plasma with temperature varying from over 5 eV down to about 1 eV.

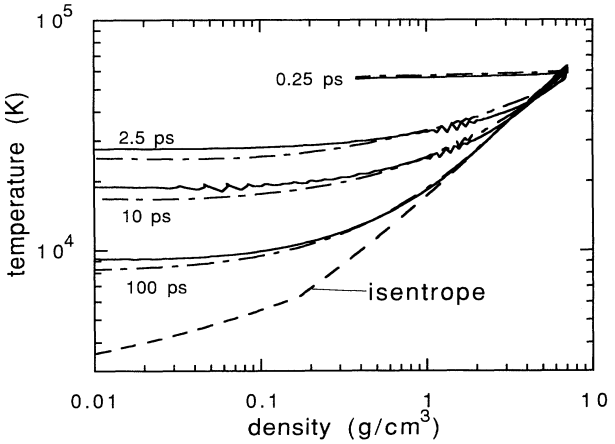

FIG. 5. Density-temperature plot showing the effect of thermal conduction on the release states at various times after the shock release. The isentrope is shown by the dashed curve. Two curves are shown for each of a series of times showing results of calculations made with Rinker's thermal conductivity (solid) and the thermal conductivity from Lee and More's model (dash-dot). The small temperature oscillations are artifacts of the numerical solutions.

In the interest of maintaining a consistent description of the release wave, electrical and thermal conductivities from each of the two models discussed above (Lee and More or Rinker) were always used together (thermal conductivity in calculating the release profiles and electrical conductivity in computing the reflectivity and emission). Two curves are shown in Fig. 5 for each time. These show the difference between calculations using thermal conductivities from the model by Lee and More (dot-dash), and that due to Rinker (solid). Despite the large differences in the electron-ion collision rates predicted by the two transport models over much of the density-temperature plane, as evidenced in Fig. 4, there is remarkably little difference in the predicted temperature profiles. The reason lies in the fact that the crucial parameter which governs this process is the value of the thermal conductivity in the hot shock-compressed Hugoniot state. Both transport models tend to agree fairly well in this region; they both predict nearly the same electrical and thermal conductivities along the Hugoniot curves, and therefore both result in very similar temperature profiles. Most of the heat that is injected into the rarefaction flows out of the shock-compressed region during the very short time scale given by Eq. (6), when the rarefaction wave scale length is very short. At subsequent times those plasma elements which were affected by the initial heat injection expand nearly isentropically, with trajectories spanning a continuum of isentropes that lie above the isentrope passing through the Hugoniot state. As the wave expands, more and more material is entrained in the wave, and the relative amount of material contained in the heated fraction diminishes, resulting in curves that slowly approach the limiting isentrope. For correct analysis of the release process, it is necessary to compute the profiles numerically including the effects of thermal conduction since there is no simple analytical model that can produce the profiles accurately. However, a good assessment of thermal conduction heating in the release wave requires an accurate value for the thermal conductivity only along the Hugoniot curve, and not over the entire density-temperature plane.

III. OPTICAL PROBING OF THE EXPANDING PLASMA

A. Electromagnetic wave propagation

At very early times in the shock-release process the rarefaction wave contains very steep density gradients, yielding a nearly steplike spatial variation in the optical properties. For such steep gradients an optical probe will pass through the low-density vapor cloud and interact with the high-density material, reflecting at the critical density layer where the plasma frequency equals the optical frequency. The magnitude of the density gradient at

early times (10–100 ps) after the shock breakout can be appreciated by examining Fig. 3 which represents a snapshot at 100 ps. Here the mass density drops exponentially by three orders of magnitude over a spatial scale length of about 5 μm. The electron density profile will be even steeper because of recombination in the greatly expanded regions where the ionization state drops to values near zero. The gradient scale length in the rarefaction wave is proportional to the time elapsed after release. Thus at earlier times the gradients are corresponding steeper. Reflection from these steep gradients is similar to Fresnel reflection, but since the gradient scale length is of the order of one wavelength, effects due to the structure of the gradient must be taken into account.

We examine the optical probing process by solving the classical turning point problem of an electromagnetic wave reflecting from a density gradient containing a critical density layer. A similar problem has been studied recently by several authors [39–41] in the context of dense laser-produced plasmas on subpicosecond time scales. The technique for solving this problem is well known [42] and will only be summarized here. The geometry of the problem is shown in Fig. 6, in which the Maxwell equations are solved in a Cartesian coordinate system. The z axis is oriented opposite to the density gradient, denoted by the unit vector $\hat{\mathbf{z}}$ which is normal to the expanding surface. The plane of incidence is in the y-z plane. We consider a plane wave propagating into the gradient with angle of incidence θ and an equal angle of reflection. We also define a unit vector $\mathbf{\Omega}$, which is directed along the reflected beam. We assume that the magnetic permeability in the plasma is $\mu=1$, and that the dielectric function ϵ is described by the Drude model,

$$\epsilon(z)=1+i\frac{4\pi\sigma(\omega,z)}{\omega}\ , \tag{7}$$

where $\sigma(\omega,z)$ is the frequency-dependent Drude conductivity given by Eq. (5), which varies throughout the plasma profile. In the discussion that follows the angular frequency of the optical probe is $\omega=2\pi\nu=2\pi c/\lambda$ and the vacuum wave number is $k_0=\omega/c$, where c is the speed of light in vacuum. The Poynting vector of the incident wave is $\mathbf{Y}_{i\lambda}$ where the subscript i denotes the polarization state (s and p).

For s polarization, $E_y=E_z=H_x=0$, where E_y and E_z are the y and z components of the electric field vector, and H_x is the x component of the magnetic field vector. In this case the Maxwell equations lead to the following differential equation:

$$\frac{d^2U}{dz^2}+k_0^2(\epsilon-\sin^2\theta)U=0\ , \tag{8}$$

where $U(z)$ is the amplitude of the x component of the electric field vector, $E_x=U(z)\exp[-i(\omega t-k_0 y\sin\theta)]$. The other two components of the magnetic field vector can be found once E_x is solved for. For p polarization the magnetic field component is perpendicular to the plane of incidence, so that $H_y=H_z=E_x=0$, and the resulting equation is

$$\frac{d^2V}{dz^2}-\frac{d[\log\epsilon]}{dz}\frac{dV}{dz}+k_0^2(\epsilon-\sin^2\theta)V=0\ , \tag{9}$$

where $H_x=V(z)\exp[-i(\omega t-k_0 y\sin\theta)]$ is the x component of the magnetic field vector in the wave. E_x and E_y are easily found once the solution for H_x is known.

In each case, the integration of these equations leads to two independent particular solutions which can be used to construct the spatial profile of the electromagnetic

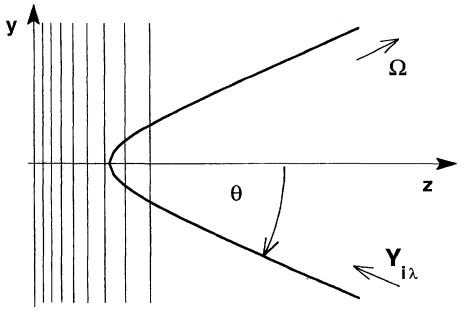

FIG. 6. Sketch of the geometry used in calculating the interaction of an electromagnetic wave with the plasma gradient.

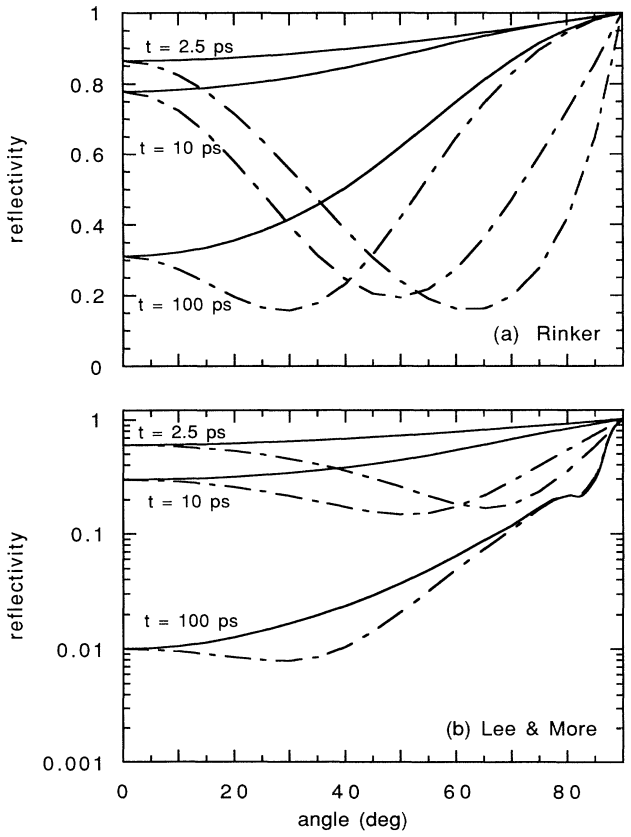

FIG. 7. Angular dependence of s- and p-polarized reflectivities at wavelength $\lambda=570$ nm. Solid curves are s-polarized reflectivities and dash-dot curves are p-polarized reflectivities. The upper and lower frames show results calculated with Rinker's and Lee and More's conductivity models, respectively, at three different times after the shock release.

wave along the plasma gradient. These solutions are conveniently described by a 2×2 characteristic matrix which can be constructed to describe the optical properties of a given slice within the plasma gradient. The profile can be modeled as a series of slices, and the characteristic matrix of the entire profile can be constructed from the product of the set of matrices. The solution is obtained by satisfying the appropriate boundary conditions. For s polarization the electric field amplitude in the vacuum is composed of an incident and a reflected wave, $U(z)=E_i\exp(-ik_0z\cos\theta)+E_r\exp(ik_0z\cos\theta)$, where E_i and E_r are the field amplitudes of the incident and reflected waves, respectively. The field transmitted into the dense shock-compressed material (with complex dielectric constant ϵ_{shock}) is $U(z)=E_t\exp[-ik_0z(\epsilon_{\text{shock}}-\sin^2\theta)^{1/2}]$, which represents an exponentially decaying evanescent field which reaches a small amplitude within a few optical depths of the critical density layer. Similar expression involving H_i and H_r for the incident and reflected magnetic field amplitudes are used to describe $V(z)$ for the case of p polarization. From the wave solutions one can define the electric vector within the wave profile, $\mathbf{E}_{i\lambda}(\theta)=E_x\hat{\mathbf{x}}+E_y\hat{\mathbf{y}}+E_z\hat{\mathbf{z}}$. The parameters i, λ, and θ indicate that, in general, the solution depends on the polarization state i (i.e., s or p), wavelength λ, and angle of incidence θ.

The reflectivity of the entire plasma profile is obtained from the incident and reflected wave amplitudes, $R_{s\lambda}(\theta)=|E_r|^2/|E_i|^2$ and $R_{p\lambda}(\theta)=|H_r|^2/|H_i|^2$ for s and p polarizations, respectively. As the plasma expands a strong reflection from the critical density layer persists. The magnitude as well as angle and polarization dependences of the reflectivity are sensitive to the conductivity.

Figure 7 shows snapshots of the angular dependence of both s and p-polarized reflectivities at various times during the release process. Results calculated with Rinker's conductivity model are presented in Fig. 7(a), while those calculated with Lee and More's model are give in Fig. 7(b). In both cases the angular dependence of the p-polarized reflectivity shows a minimum at an off-normal angle. The location of this minimum shifts from large angles to small angles with increasing time, as the scale length of the release wave increases. The reflectivity minimum is related to the driving of a plasma mode at the critical density layer, which is in resonance with the incident optical radiation. For both conductivity models this resonance is damped, although in Rinker's model it is somewhat underdamped since $\omega\tau_{ei}>1$, while with Lee and More's conductivity it is overdamped. It is evident that the reflectivity computed with Lee and More's conductivity model decreases much faster with time than that calculated with Rinker's model, over the entire angular range. This is a direct result of the much higher collisionality ($\omega\tau_{ei}<1$) in Lee and More's model as compared with Rinker's model.

B. Absorption and emission

The total absorption in the expanding plasma profile, $A_{i\lambda}(\theta)$, is easily obtained from the relation $A_{i\lambda}(\theta)=1-R_{i\lambda}(\theta)$ where $R_{i\lambda}(\theta)$ is the total reflectivity. Alternatively, to find the deposition of energy within the plasma profile we note that the absorption per unit volume is given by $\frac{1}{2}\mathrm{Re}(\sigma)|\mathbf{E}_{i\lambda}(\theta)|^2$. Integrating over the entire profile we obtain

$$A_{i\lambda}(\theta)=\int_{-\infty}^{\infty}\frac{\frac{1}{2}\mathrm{Re}(\sigma)|\mathbf{E}_{i\lambda}(\theta)|^2}{|\mathbf{Y}_{i\lambda}\cdot\hat{\mathbf{z}}|}dz\ . \tag{10}$$

The absorbed energy is normalized to the component of the incident flux which is directed into the surface normal $\hat{\mathbf{z}}$. As a check we have verified for all of our calculations that $A_{i\lambda}(\theta)=1-R_{i\lambda}(\theta)$ to better than 0.1% precision.

We can examine the integrand in Eq. (10) to obtain a detailed picture of the distribution of absorbed energy within the plasma profile. For this purpose we define an energy absorption rate, $\alpha_{i\lambda}(z)=dA_{i\lambda}(\theta)/dz$, which gives an absorption per unit length (oriented along the z axis), for radiation incident on the plasma profile. It should be noted that $\alpha_{i\lambda}$ describes absorption from both the incident and reflected waves and therefore depends on the details of the particular wave interacting with the gradient. Figures 8 and 9 show the spatial profiles of density and temperature, as well as the distributions of energy absorbed in the profile indicated by the effective absorption rate for various cases. Figure 8 corresponds to $t=10$ ps, early in the expansion process when the release profile is quite steep and the absorption is distributed over a large range of densities. In Fig. 9 the same information is shown for a later time, $t=100$ ps, when the profiles have expanded significantly (a factor of 10). In both cases all of the absorption is localized in space around the critical density layer in the plasma profile over a spatial extent of roughly one-half wavelength of the incident radiation. At the earlier time the absorption profile spans a large range of mass densities, roughly over a decade of 0.1–1.0 g/cm^3. At the later time the absorption profile has become much more localized in a narrower mass density range as the density gradient scale length increases. The centroids of this localized mass density range is dependent on the ionization state model, which determines the location of the critical density layer. The figure show results for both normal incidence and 45° angle of incidence. The p-polarized wave drives a plasma oscillation at the critical density layer, giving rise to a prominent peak in the absorption profiles. This is most evident in the case of Rinker's conductivity model, where the electron-ion collision rate is significantly smaller than the optical frequency. Such a peak is also evident in Lee and More's model at 10 ps, but not at 100 ps, because collisional damping is much stronger in this model.

The critical density layer in the plasma profile plays the role of being both a reflecting and an absorbing and/or emitting layer. Since it is reflecting (i.e., its thermal emissivity is <1), it screens emissions from deeper layers. Moreover, emissions from the lower-density plasma are low owing to the low material density. Hence we would expect the observed thermal emissions to originate primarily in the critical density layer. Because of the effects of reflection and refraction, one cannot treat the radiation emission from the plasma profile

using the radiative transfer equation that is usually applied to rarefied plasmas. This is because the radiative transfer equation assumes no refraction (refractive index equal to unity) and that absorption and emission can be described with an absorption coefficient dependent only on the local material state. Instead, we calculate the emission from the absorption profiles using an application of Kirchhoff's law in conjunction with the electromagnetic wave solutions outlined above. This procedure automatically takes into account the details of reflection, refraction, and absorption, and therefore it gives the correct thermal emissivity of the critical density layer. Kirchhoff's law applied to a reflecting metal surface at normal incidence states that [42]

$$\frac{S}{A}=I_\lambda(T)=\frac{2hc^2}{\lambda^5}\frac{1}{e^{hc/\lambda kT}-1}\ , \tag{11}$$

where S and A are, respectively, the radiated spectral intensity and absorption of the material surface, and $I_\lambda(T)$ is the radiative spectral intensity (per unit wavelength) of a blackbody at temperature T and wavelength λ. We generalize this particular case to take into account the polarization dependence and also an oblique angle of observation. Specifically the radiative power emitted at an angle θ with respect to the surface normal in a polarization state i is directed with the flux vector $\mathbf{S}_{i\lambda}=\frac{1}{2}A_{i\lambda}I_\lambda(T)\mathbf{\Omega}$, where we have included a factor of $\frac{1}{2}$ to account for the fact that we are treating each polarization state separately. In general, since $A_{i\lambda}=1-R_{i\lambda}$ is polarization dependent, the emission will also be polarization dependent. The flux emerging from the emitting surface is given by $S_{i\lambda}(\theta)=\mathbf{S}_{i\lambda}\cdot\hat{\mathbf{z}}$, thus we have

$$S_{i\lambda}(\theta)=\tfrac{1}{2}A_{i\lambda}(\theta)I_\lambda(T)\cos\theta\ . \tag{12}$$

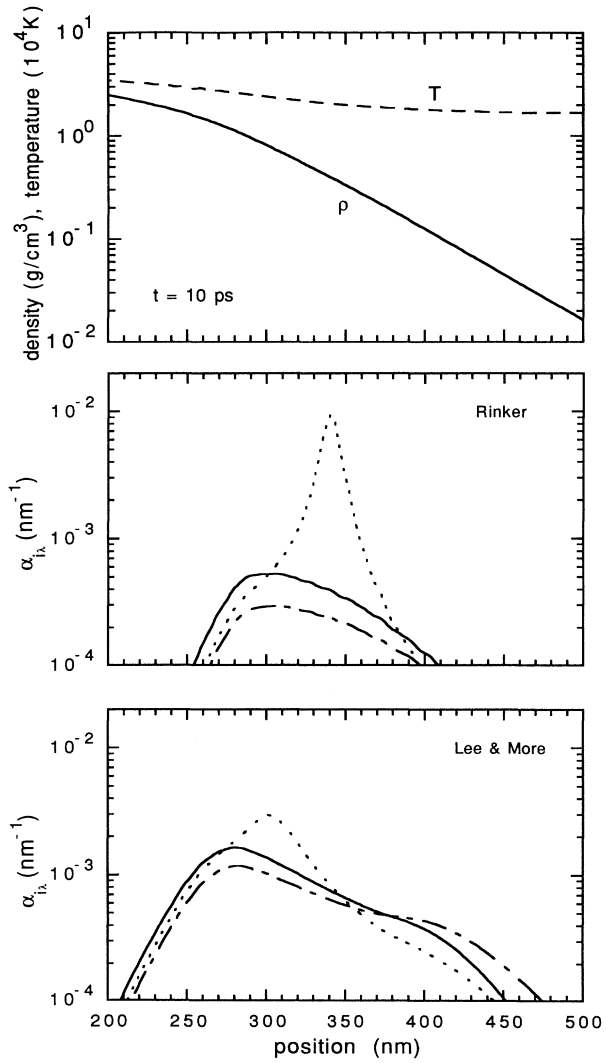

FIG. 8. Comparison of absorption profiles computed with Rinker's and Lee and More's conductivity models at time $t=10$ ps after shock release at optical wavelength $\lambda=570$ nm. The top frame shows the density and temperature profiles as a function of position, the other two frames show the effective absorption coefficient for three cases: solid curve, normal incidence; dotted curve, p polarization at 45° angle of incidence; dash-dot curve, s polarization at 45°.

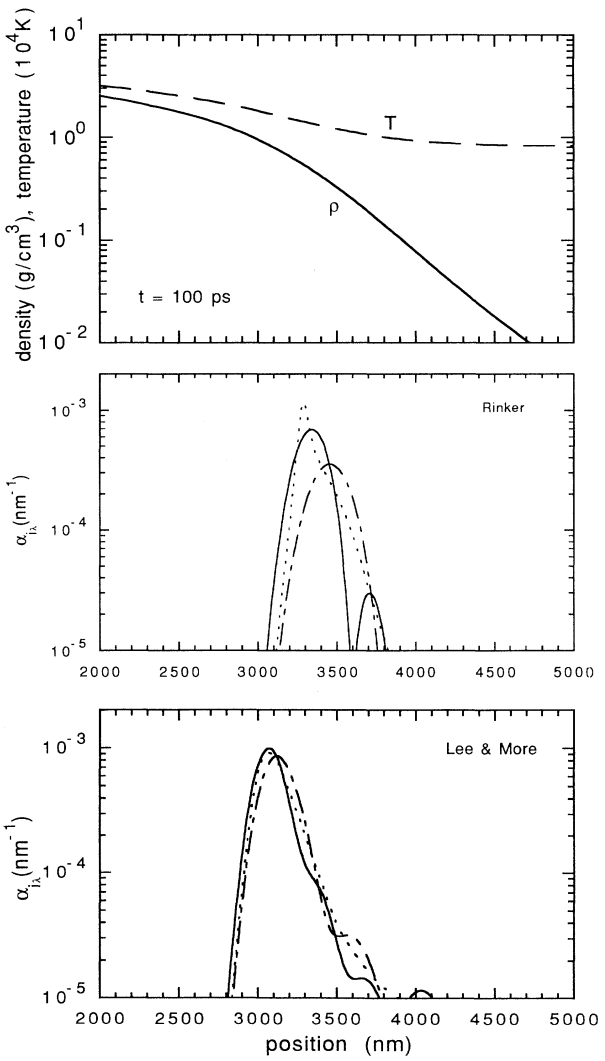

FIG. 9. Same as Fig. 8, but for time $t=100$ ps after shock release.

If the entire plasma profile were isothermal at temperature T then Eq. (12) would be sufficient to compute the emission. However, the temperature gradient within the profile requires a generalized form of Eq. (12),

$$S_{i\lambda}(\theta)=\lim_{z\to\infty}\left\{\int_{-\infty}^{z}\tfrac{1}{2}\alpha_{i\lambda}(z')I_{\lambda}(T(z'))\cos\theta dz'\right\}. \quad (13)$$

This amounts to the statement that each plasma layer dz' at location z' within the plasma profile contributes an emissive intensity which is proportional to $I_{\lambda}(T(z'))$ and to the local absorption rate experienced by the layer for the equivalent wave incident from the vacuum.

Throughout the release process the thermal emission originates from a limited range of densities in the plasma profile. Plotted in Fig. 10 are locii of density boundaries of the plasma region yielding 80% of the total emission. These boundaries are determined by locating the z coordinates (and hence the densities and temperatures) for which the integral in Eq. (13) attains 10% and 90% of its asymptotic value for $z\to\infty$. The boundaries corresponding to emissions at three different wavelengths are traced out over time, following the cooling of the plasma profile from about 5 to 1 eV in the duration of 2.5–200 ps for which the trajectories are shown (compare to Fig. 5). To aid in interpretation, density-temperature curves for the release profiles at $t=2.5$, 10, and 100 ps are also shown. For early times, when the temperatures are higher, the emission originates over a broader range of densities, with the upper density bound reaching values approaching that of the Hugoniot state. The emission zone rapidly narrows to an extent spanning about a factor of 2 in density ranging about 0.3–0.7 g/cm^3 for Rinker's model, and 0.6–1.0 g/cm^3 for Lee and More's model. The density from which the emission originates depends on the wavelength, with longer wavelengths being emitted from lower densities. Finally, we note that the temperatures also approach a limiting value. Within the time scale of interest in this study, $t=10$–100 ps, the temperature profile spans a region of about 1–2 eV. Thus the density-temperature region responsible for optical absorption and thermal emission is effectively localized to a relatively narrow range of densities and temperatures, spanning a region of roughly a factor of 2 in each variable. Analyses of the emission regions have also been made for a range of observation angles, polarizations, and wavelengths. These yield diagrams similar to that presented in Fig. 10. This is not surprising since, as already indicted in the Introduction, the location of the emitting region is determined essentially by the release isentrope and its intersection with electron densities giving plasma frequencies equal to the frequencies of the radiation of interest.

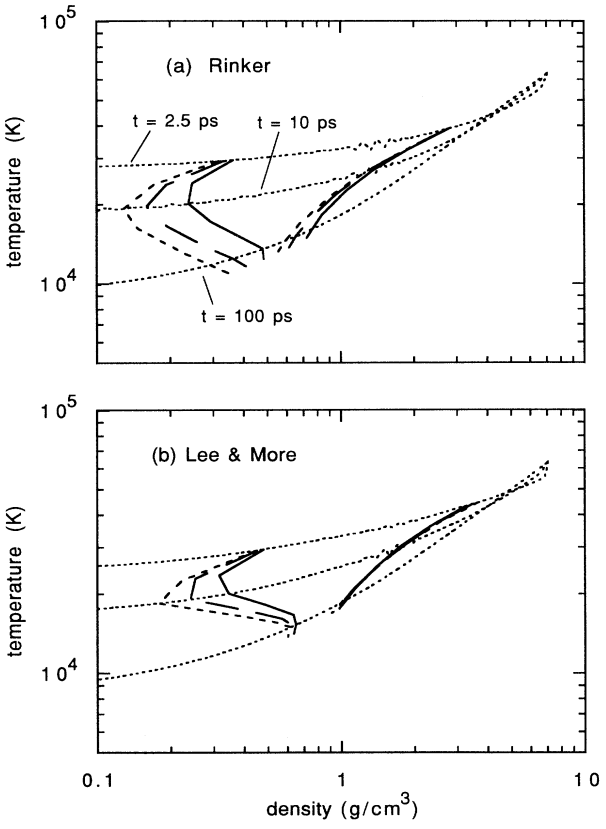

FIG. 10. Localization within density-temperature space of thermal emission within the release profile. Each pair of curves (heavy lines) represents density-temperature coordinates for the 10% and 90% levels of the total emission integral [Eq. (13)]. Solid curves $\lambda=430$ nm, long dashes 570 nm, short dashes 690 nm. The curves span a time range of 2.5–200 ps. Emission originates along a curve determined by the time-dependent density-temperature profile spanning the region between these two bounding curves. Snapshots of such curves (light dotted lines) at $t=2.5$, 10, and 100 ps are indicated in the figure.

C. Applicability of the Drude model

The results of the previous sections show that the reflection from the critical density layer in the plasma profile is the dominant process which determines both the reflectivity and the thermal emissivity of the release wave at early times. The validity of this result depends heavily on the validity of the Drude description for the dielectric function. For condensed matter, the Drude model breaks down because it takes no account of electronic structure effects, namely, contributions to the optical properties from interband transitions and modifications to the electron dynamics due to the shape of the Fermi surface. The picture is, however, considerably simplified for liquid metals where the disordered state washes out much of the band structure and the optical properties can be fitted remarkably well to a simple Drude model [43]. For aluminum shock melting occurs at approximately 1.2 Mbar on the Hugoniot curve [44], hence for the strong shock and release process (10 Mbar) considered in this study the microscopic state is mainly that of a disordered fluid. We expect a Drude model to be applicable for the dense Fermi-degenerate regions along the release isentrope, namely, for densities larger than about 1 g/cm^3. It is likely that a more complicated frequency-dependent description which takes into account some of the emerging electronic structure as the density decreases is necessary for the expanded states of <1 g/cm^3. However, no such model is currently available.

D. Effect of the vapor screening layer

As pointed out in Sec. I, optical probing of the expanding plasma in a release wave may be hindered by the low-density vapor in the tail of the rarefaction wave. For this low-density vapor, the Drude model does not provide an adequate description of the plasma opacity. The Drude model describes the low-frequency limit of electron-ion collisional absorption (or bremsstrahlung absorption), and within the context of the theory of ideal plasmas it is valid for $h\nu \ll kT$ [45]. This limit ensures that the atomic shell structure plays no role in absorption or emission (bound-bound or free-bound transitions) at the optical frequencies of interest. However, for plasma temperatures of around 1 eV (compared with optical photon energies of 2–3 eV) as examined in this study, this condition is violated. Under these conditions highly excited valence states in the hot vapor can also participate in the absorption and emission process. This is the source of opacity in the low-density partially ionized vapor cloud that forms a screening layer in the tail of the rarefaction wave [16].

A simple expression for the opacity of this vapor, which takes into account both free-bound transitions and electron-ion scattering (bremsstrahlung) in the outer valence states, is given by the Kramers-Unsöld formula [46],

$$\kappa_\nu(n_i,T)=0.96\times10^{-7}\frac{n_i Z^2}{T^2}\left\{\exp\left[\frac{-(I-h\nu)}{kT}\right]\right\}\times\left[\frac{kT}{h\nu}\right]^3 \text{cm}^{-1}, \tag{14}$$

where the numerical coefficient applies when the ion density n_i is expressed in units of cm^{-3}, and the temperature T in K. I is the ionization energy of the dominant ion species. This formula is valid for photon energies $h\nu < I$, and becomes invalid for photon energies large enough to ionize atoms in the ground state. This opacity is strongly temperature dependent, due to the exponential Boltzmann factor, and is an increasing function of temperature. The Kramers-Unsöld formula is based on hydrogenic model for the atomic levels in the ion, and breaks down in the high-density limit.

By folding the opacity formula into the density profile and integrating to yield an optical depth along the profile, one can estimate the screening effect of the low-density vapor layers. Specifically, we can develop a criterion for the time scale t_s during which the low-density vapor cloud expands to a sufficient size to screen the critical surface layer. The density profile in the low-density tail can be characterized with an exponential fit (see Fig. 3), and for $n_i < 2\times10^{21}$ cm^{-3} ($\rho < 0.1$ cm^3) is given approximately by

$$n_i(z,t)=\tilde{n}_i \exp\left[-\frac{z-\tilde{z}}{\tilde{c}_s t}\right] \quad \text{for } z>\tilde{z}, \tag{15}$$

where $\tilde{n}_i=2\times10^{21}$ cm^{-3}, $\tilde{c}_s$ is the speed of sound in the rarefaction wave in the low-density tail, and $\tilde{z}(\tilde{u}-\tilde{c}_s)t$ marks the moving point in the profile where $n_i=\tilde{n}_i$ ($\tilde{u}$ is the particle speed at the point $\tilde{z}$). The sound speed is approximately constant because the temperature profile in the rarefaction tail is nearly isothermal (see Fig. 3). For our estimates we assume a value of $T=10\,000$ K (which leads to a conservative estimate for the t_s). The optical depth of the screening layer is then given by

$$\tau_{\text{opt}}=\int_{\tilde{z}}^{\infty}\kappa_\nu(n_i,T)dz = 0.96\times10^{-7}\tilde{c}_s t\frac{\tilde{n}_i Z^2}{T^2}\exp\left[\frac{-(I-h\nu)}{kT}\right]\left[\frac{kT}{h\nu}\right]^3. \tag{16}$$

In evaluating this expression we have assumed that the main variation in the opacity along the density gradient is due to the density itself, since the temperature is nearly constant. The expression for τ_{opt} increases linearly with time. This is characteristic of self-similar expansion, in which the density profile maintains a constant shape but expands in scale at a constant rate. The dominant ion species is neutral monatomic aluminum, for which the appropriate value for Z is 1 in Eq. (16) and the ionization energy is $I=5.99$ eV. We integrate up to the layer where the Drude model predicts most of the absorption to occur, i.e., to $\rho=0.1$ g/cm^3. In the rarefaction wave tail the sound speed is $\tilde{c}_s=3.5\times10^5$ cm/s. The screening effect of the opaque low-density value tail becomes important when τ_{opt} approaches unity. Substituting into Eq. (16) the values for $\tilde{c}_s$ and $\tilde{n}_i$, and assuming a photon energy in the visible with $h\nu=2.5$ eV, we find that $\tau_{\text{opt}}(t_s)=1$ corresponds to a characteristic time of $t_s=2000$ ps for developing an opaque screening layer. Similar values are obtained for other photon energies of the visible spectrum. Thus the time scale of 10–100 ps pertinent to this study is consistent with the criterion $t \ll t_s$.

IV. RESULTS AND DISCUSSION

A. Reflectivity and emission

The analysis presented above leads to a series of predictions that can be tested experimentally. The localization of the reflection and emission in the release wave allows one to obtain experimental measurements which are sensitive to the conductivity and ionization state in a region of the density-temperature plane located around 0.2–1.0 g/cm^3 and 10 000–20 000 K. In this section we identify a few characteristic features in the angle and polarization dependence of both the reflectivity and the emission.

We compare in Fig. 11 the temporal dependence of the reflectivity at various angles of incidence for both conductivity models. These results reveal significant differences between the models. For Lee and More's model, which is more collisional, the normal incidence reflectivity decreases monotonically at a rate of around 0.05 ps^{-1} while with Rinker's model the rate of decrease is much slower at 0.01 ps^{-1}. A similar behavior is seen for s polarization at other angles of incidence, with the main effect being a reduction in the rate of reflectivity de-

crease with increasing angle of incidence. This exponential decay may be understood qualitatively from the WKB solution for normal incidence light interacting with a plasma gradient in the long scale-length limit. In the idealized case of an isothermal profile, an electron-ion collision rate proportional to electron density, and either a linear or exponential spatial density profile with scale length L, the WKB result predicts a reflectivity proportional to [41] $\exp(-A^*\nu_{ei}^*L/\lambda)$. Here $\nu_{ei}^*=1/\omega\tau_{eic}$ is the electron-ion collision rate at critical density, $1/\tau_{eic}$, normalized to the light frequency ω. The constant A^* has a value of 13.4 (16.8) for a linear (exponential) density profile. For the shock-released state the profile is most nearly exponential with scale length $L=c_st$ that expands linearly with time, where c_s is the sound speed. This linear scale expansion produces the exponential reflectivity decay. Also apparent from this analysis is the fact that the decay rate is proportional to ν_{ei}^*, i.e., inversely proportional to the plasma conductivity. Quantitative analysis using this idealized WKB result is not viable because the true profile is not isothermal, and the density dependence of the collision rate is more complicated than assumed in the simple formula above. Thus close examination of the calculated reflectivity decay shows that the decay is not perfectly exponential. However, this simple qualitative picture is useful in assessing comparisons of experimental data with model calculations.

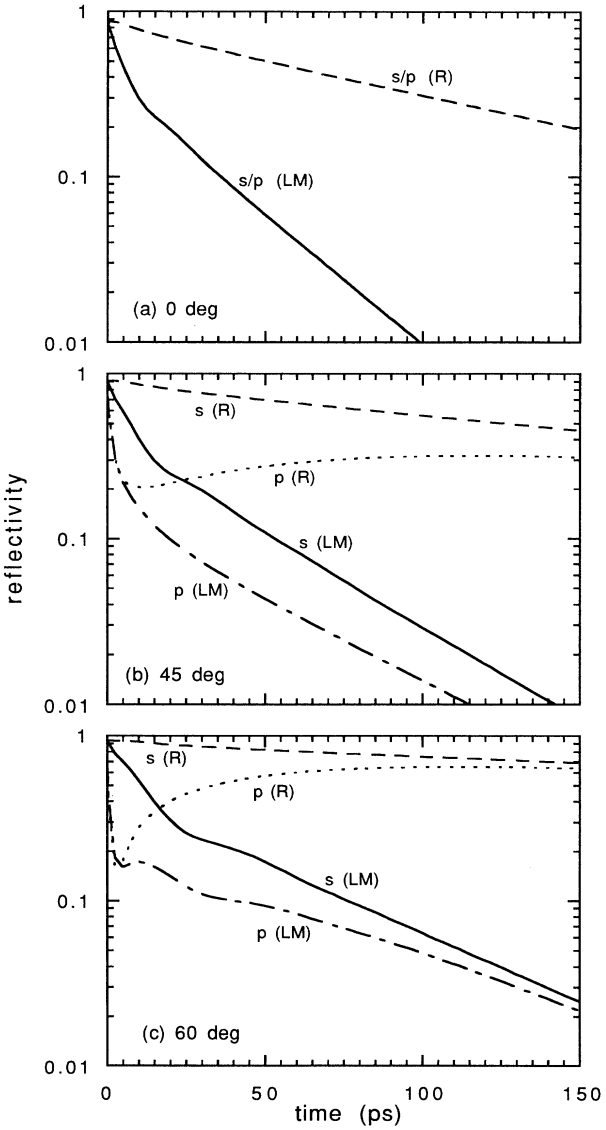

FIG. 11. Time dependence of reflectivity at three angles of incidence and optical wavelength $\lambda=570$ nm. The dashed and dotted curves are s- and p-polarized reflectivities, respectively, calculated with Rinker's model. The solid and dash-dot curves are s- and p-polarized reflectivities, respectively, calculated with Lee and More's model.

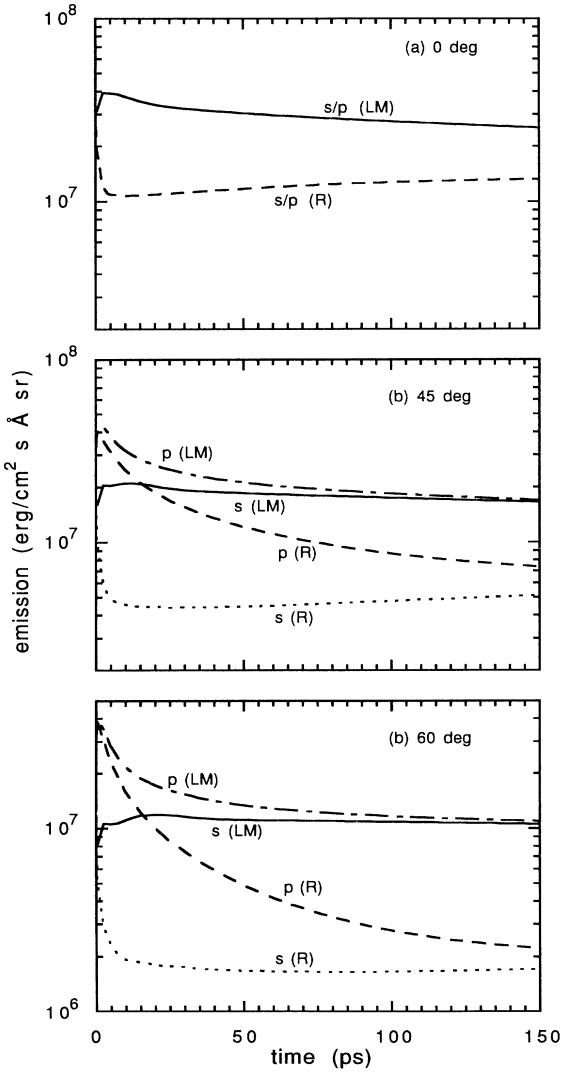

FIG. 12. Time dependence of emission at optical wavelength $\lambda=570$ nm and at three angles with respect to the normal. The dashed and dotted curves are s- and p-polarized reflectivities, respectively, calculated with Rinker's model. The solid and dash-dot curves are s- and p-polarized emission, respectively, calculated with Lee and More's model.

For p polarization the reflectivity is lower than that of s-polarized light due to the excitation of the plasma resonance in the release profile. In addition, depending on the electron-ion collision rate, a nonmonotonic temporal evolution of the p-polarized reflectivity may result in the case of Rinker's conductivity model. For Rinker's conductivity, $\omega\tau_{ei} > 1$, and the plasma resonance accounts for a significant fraction of the p-polarized absorption at early times. It manifests itself in the large peak displayed in the absorption profiles shown in Fig. 8. As noted previously, another manifestation of this resonance is the large minimum in the angular dependence of the reflectivity, which shifts as a function of time. As the profile expands, the minimum in the reflectivity shifts to smaller angles as the scale length of the profile increases. This causes the p-polarized reflectivity to decrease, and then subsequently to increase as the minimum shifts through the observation angle. For Lee and More's conductivity, $\omega\tau_{ei} < 1$, and the plasma resonance is at all times overdamped. The difference between s and p polarization does not result in nonmonotonic temporal behavior, although there is some residual structure in the p-polarization time dependence.

An important complement to the reflectivity measurement are observations of the plasma emission. The combined measurements of both provides a strong consistency check on the theoretical models. Shown in Fig. 12 are curves for the temporal evolution of the plasma emission at 0°, 45°, and 60° incidence. In general, Rinker's model with higher conductivity predicts higher reflectivity and lower emission intensities than Lee and More's model. The difference between the emission intensities for the two models varies between a factor of 2 and 4 for observations normal to the free surface and a factor of 8 at oblique angles (60° from the normal) of observation. At late times the s- and p-polarized emissions converge to similar values.

In Fig. 13 we show detailed results of the angular dependence of the emission for both polarization states. This information might be obtained experimentally with a fairly simple arrangement such as angle-resolved streak pyrometry. The top frames show the angular dependence at time $t=0$ ps (at the moment of shock release). This time zero calculation is presented for completeness only. Such a measurement cannot be made, since the state becomes obscured by the lower-density material within 1 ps of the release. Here both Lee and More's model and Rinker's model predict similar conductivities and the calculated results are thus similar. At early times during the shock release the p-polarized component is strongly enhanced at oblique angles of observation consistent with the diminished reflectivity at these angles. One may note how the large enhancement in p-polarized emission relative to s-polarized emission evolves with time. As noted above, the strong enhancement in emission is related to the plasma resonance at the critical density layer. A

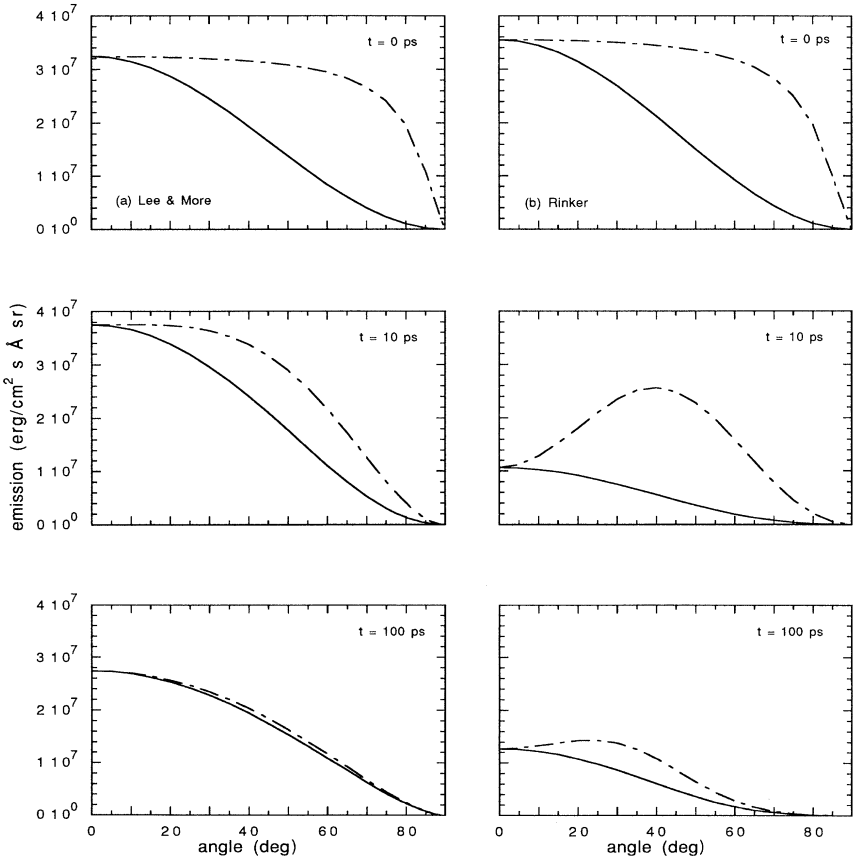

FIG. 13. Angular dependence of emission at optical wavelength $\lambda=570$ nm. Comparison of the emission computed with (a) Lee and More's and (b) Rinker's conductivity models, respectively. Solid curves are for s-polarized emission, and dash-dot curves for p-polarized emission. Emission is shown at three different times after the shock release.

much stronger asymmetry between the s- and p-polarized emission components at oblique angles is found for Rinker's conductivity model. Such an asymmetry is thus a characteristic of high conductivity, that is, $\omega\tau_{ei} > 1$. This may be contrasted with the results calculated using Lee and More's model, in which the enhancement of p-polarized emission is less significant and almost disappears entirely by $t = 100$ ps. For late times the angular distribution of the emission calculated with Lee and More's conductivity is almost Lambertian, with emissivity approaching unity.

B. Temperature determination

The results presented here are all based on a combination of several theoretical models, specifically the equation-of-state and conductivity models, as well as the assumption of a Drude model for the frequency dependence of the conductivity. The models used in these calculations are uncertain to some degree. For example, the predicted temperatures in the expanding profile differ by a magnitude of up to 30% depending on the EOS, as previously discussed in Sec. II A, and shown in Fig. 3. Therefore it is important to extract experimental information that is, as far as possible, independent of theoretical models. An accurate experimental determination of the temperature within the emitting and absorbing plasma layer could provide important information for improving theoretical models. We describe next how this may be possible by combining the results of a time-resolved reflectivity measurement with those of a time-resolved emission measurement. This method exploits the fact that the optical absorption and emission are both localized to the same region in the plasma profile, in much the same way as reflection and absorption are localized to the skin depth layer of hot solid metal surface.

Experimental measurements of temperature in unloading plasmas have been made previously, based on a spectral fit of an observed thermal spectrum using a gray-body function [10,15]. This method assumes a wavelength-independent thermal emissivity, which is generally not true over the visible range. Alternatively, brightness temperature measurements, which use absolute emission levels, will not indicate the true temperature of the material if the thermal emissivity of the emitting layer is small (or unknown). A key improvement is to use a measurement of reflectivity at the emission wavelength to infer the thermal emissivity. Accurate reflectivity measurements should be possible as long as the initial surface is of optical quality, and the shock front is smooth and planar. The plasma profile behaves much like a specularly reflecting metal surface, where the emissivity of the reflecting layer can be obtained purely from the corresponding reflectivity through the relation (for normal incident) $\varepsilon = 1 - R$, where ε is the emissivity and R is the (experimentally measured) reflectivity. To infer a temperature we use Eq. (11), replacing S and A, respectively, with the measured emission intensity, and with ε inferred from reflectivity measurements at the same wavelength. This leads to the equation (for normal incidence, unpolarized radiation)

$$\frac{S_{\text{expt}}(t)}{1-R_{\text{expt}}(t)} = \frac{2hc^2}{\lambda^5}\frac{1}{e^{hc/\lambda k T_{\text{expt}}(t)}-1} . \tag{17}$$

Implicit in this analysis is the assumption that no other processes (e.g., scattering or absorption in the low-density vapor) are significantly present to modify the observed reflectivity. At early times in the release the emission and reflection are not localized in a narrow density range. However, due to the isothermal nature of the wave profile at these early times it is clear from Fig. 5 and 10 that the emission is localized in a narrow range of temperatures.

As a check on this procedure we show in Fig. 14 a plot of temperatures "inferred" from the absolute emission levels and reflectivity calculated using both conductivity models. The top frame shows results obtained with Rinker's model, and the bottom frame with Lee and More's model. A set of error bars is plotted on each frame. The upper and lower bounds of these error bars show the temperature spread within the central 80% of the emitting region. These temperature bounds correspond to temperature coordinates located on the density-

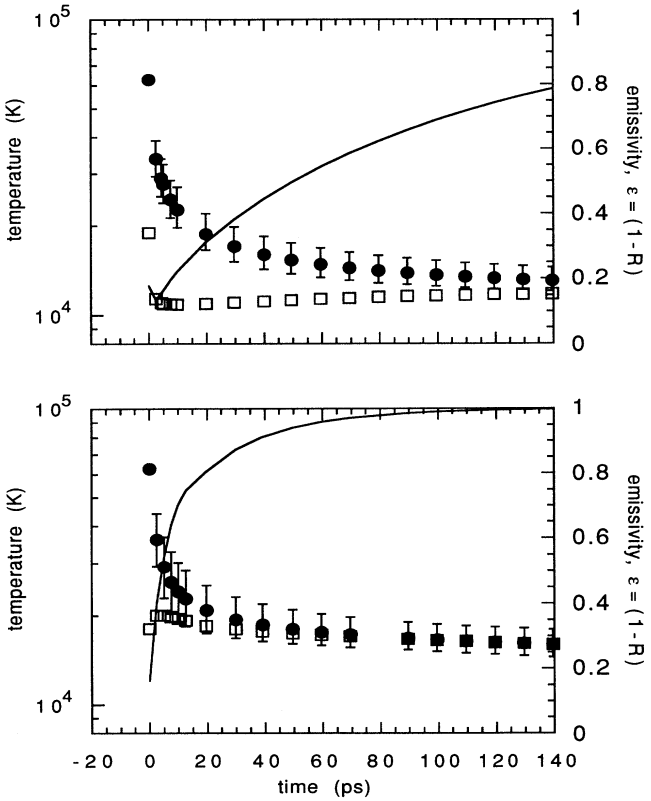

FIG. 14. Temperature assessment from reflectivity and emission measurements at optical wavelength $\lambda = 570$ nm (a) computed with Rinker's and (b) Lee and More's conductivity models. The solid symbols show temperature "inferred" from reflectivity and emission. The error bars show the temperature spread across the central 80% of the emitting region. Open symbols show brightness temperature inferred from the emission intensity, assuming an emissivity $\varepsilon = 1$. The solid curves show the emissivity $\varepsilon = 1 - R$ which is used to correct the emission intensity to obtain the "inferred" temperature.

temperature locii defined for Fig. 10, where they intersect the release curves at various times. The upper and lower temperature bounds are also associated, respectively, with the upper and lower density bounds of the emitting region. Since the emitting region is not exactly isothermal, these error bars show the precision to which a temperature measurement can be expected to yield a meaningful value. More importantly for the discussion which follows, these temperature bounds show the "true" set of temperatures spanned by the emitting layer as it evolves in time. An accurate temperature determination ought to yield mean temperatures inside this temperature span. The open symbols in the figure show uncorrected brightness temperatures, i.e., temperatures inferred from Kirchhoff's Law assuming an emissivity $\varepsilon=1$. These points differ strongly from the "true" values, especially at early times. It is clear that for release profiles that are highly reflecting, the correction for emissivity is critical for inferring an accurate temperature. The solid curves show the emissivity ε as a function of time which is used to correct the emission measurements. Finally, the solid symbols in the figure show the "corrected" temperatures. The "corrected" temperatures reflect the average temperature in the emitting region quite accurately, since they sit quite close to the average between the upper and lower bounds of the "true" temperatures. This close agreement indicates that reflectivity measurement indeed can be used to infer an effective emissivity for the purpose of correcting brightness temperature measurements. The magnitude of the correction to the emission is proportional to $1/\varepsilon$. In the case of Lee and More's conductivity the correction factor $1/\varepsilon$ is much closed to unity (hence less critical in determining temperature) since the reflectivity drops quickly to small values (<0.1 after about 30 ps for normal incidence).

C. Doppler-shift measurements

The localization of the emission and reflection to a fixed density within the plasma profile suggests that a Doppler-shift measurement of the reflected light spectrum may be used to obtain the average particle speed of the material in this layer. The density and ionization state may then be inferred using the particle speed obtained from the Doppler-shift measurements. However, inferring these latter two parameters requires some theoretical input, since an EOS is required to infer a density from the particle speed. Doppler-shifted reflections have been used in high-intensity femtosecond laser-produced plasma measurements to determine plasma expansion speeds, and hence to infer the plasma temperature [12]. We discuss next the basis for inferring these parameters from optical measurements.

In the ideal case of a perfectly isentropic release wave (centered rarefaction), all of the hydrodynamic variables are functions of the self-similar coordinate z/t. There is no explicit time dependence other than through this self-similar parameter. Hence the density and particle speed throughout the profile are related through a single time-independent monotonic function, which can be calculated easily using the equation of state of the material (along the release isentrope) using Eq. (2). The important consequence of this fact is that the particle speed associated with any given density in the release profile is a time-independent quantity, and varies smoothly throughout the release profile. Since the reflection is localized to a particular *density* layer, the average observed Doppler shift will be nearly constant in time. This function relating mass density ρ to particle speed u is shown by the solid curve in Fig. 15. This curve is derived from the isentrope passing through the 10-Mbar shock state on the Hugoniot curve in aluminum.

In the calculations we have shown here the situation is not quite so simple, because the high thermal conduction at the beginning of the release results in an initially isothermal release profile. This means that the initial particle speed u for a given density is significantly larger than that expected from an isentropic release, but relaxes quickly to smaller values. However, even at $t=100$ ps the isentropic release does not describe the ρ-u relationship adequately. The other two curves in Fig. 15 show snapshots of the ρ-u relationship at time $t=10$ p and 100 ps after the shock release. In the 0.1–1.0 g/cm^3 density range this will introduce a time-dependent correction of the order of $(0.2-0.4)\times10^6$ cm/s. Figure 16 shows a calculation of the Doppler shift $\Delta\lambda/\lambda=2u/c$ evaluated for the particle speed at critical density (at $\lambda=570$ nm and normal incidence) for both conductivity models. The different results arise from the different ionization state models. In Rinker's model the larger ionization states means that the critical electron density is located at a relatively lower mass density, and correspondingly higher particle speed. Nearly constant Doppler shifts of $\Delta\lambda/\lambda\sim2.5\times10^{-4}$ can be expected for a 10-Mbar shock in Al.

One can use the Doppler-shift measurement to infer the mass density by using a hydrodynamic simulation with a reliable equation of state and thermal conductivity

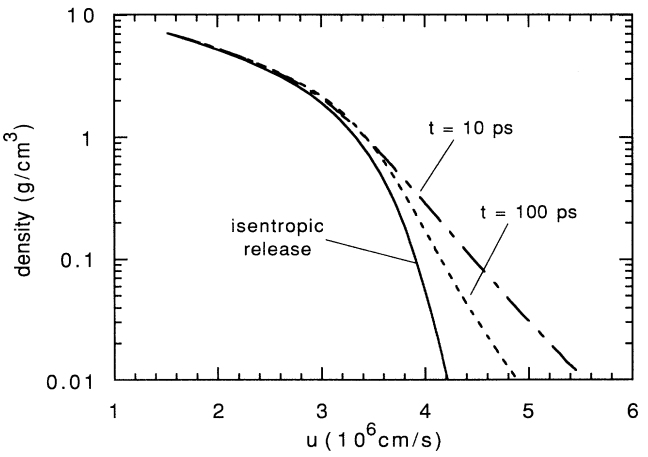

FIG. 15. Density vs particle speed in the release profile. The solid curve shows the stationary curve predicted from a perfectly self-similar isentropic flow. The dash-dot curve and dotted curve show snapshots of the ρ-u curves at $t=10$ and 100 ps, respectively, from calculations of the release profiles including the effects of thermal conduction.

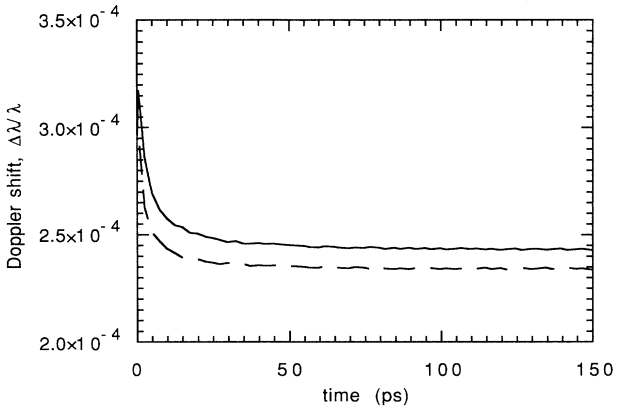

FIG. 16. Doppler shift of light reflected normally from the critical density layer for $\lambda = 570$ nm probe light, as a function of time. Results are shown for Rinker's (solid) and Lee and More's (dashed) conductivity models.

to provide an accurate ρ-u curve along the release profile. As we have shown earlier, the mechanical parameters in the release profiles calculated with the different EOS models (QEOS and SESAME) agree remarkably well, and indicate that these curves may be relatively insensitive to variations in EOS models. Furthermore, the discussion in Sec. II C indicates that an accurate assessment of thermal transport effects, which govern the time-dependent corrections, requires an accurate thermal conductivity only in the vicinity of the Hugoniot state, where current theoretical models are fairly sound. This strongly suggests the possibility of inferring accurate mass densities from the Doppler shift in reflectivity.

Inferring the ionization state from such measurements is also possible using the fact that the electron density at the reflecting layer is determined by the wavelength of the optical probe used (since the reflection occurs at the critical density layer in the profile, where the plasma frequency equals the optical frequency). The fixed and known electron density, combined with the inferred mass density, can then yield the ionization state. Further information, such as density gradients within the reflecting region, might also be inferred from the spectral width and shape of the Doppler-shifted reflected signal. This assumes, naturally, that the incident probe spectrum is sufficiently monochromatic.

Accurate calculations of the Doppler-shifted spectrum will of course require a time-dependent solution of the Maxwell equations in the moving release profile. The current calculation assumes only a static profile (no time dependence in the electromagnetic wave equations).

V. CONCLUSIONS

In the analysis presented in this study we have identified the possibilities of obtaining information on the transport properties as well as temperature, mass density, and ionization state in dense shock-released plasmas using optical measurements. These plasmas are obtained by shocking solid samples to isentropes lying above the liquid-vapor critical point. Such measurements are possible if the temporal resolution of the experiment is sufficiently high to allow the examination of the release process during times in the range of 10–100 ps after the release of the shock. On this time scale the release wave presents a very steep density gradient, in which an optical probe interacts primarily with the critical density layer. Thermal emission, absorption, and reflection will all occur predominantly at this layer, thus providing a degree of localization, in the density-temperature plane of the material state responsible for the observed optical properties.

Specifically we have shown that both emission and reflectivity measurements will exhibit characteristic dependences on time, angle of observation, and polarization state. Such dependences are all sensitive to the conductivity of the plasma. Theoretical models of plasma conductivity in the low-temperature region of dense plasma states disagree to a sufficient extent that further experimental investigations will yield new information on the subject. The basic experimental techniques for performing these measurements have already been demonstrated, although they require further refinement to address the possibilities suggested in this study. At this time, laser-driven shocks provide the most viable method for producing the strong shock pressures required for these experiments (to reach release isentropes above the critical point), and because such methods are easily adapted to the high temporal resolutions required.

Further information may be obtained by combining reflectivity and emission measurements to infer the plasma temperature within the emitting and reflecting region. Measurement of the reflected light spectrum may also lead to determination of the particle speed within this layer, and allow an assessment of the mass density and plasma ionization state with the help of an equation-of-state model. From Fig. 14 and 16 it is clear the experimental determinations of the density and temperature of the localized region of absorption and emission will yield data that are nearly constant in time from about 20 ps to more than 100 ps. A successful measurement of these parameters within this time range would provide specific experimental constraints on the density and temperature of the emitting and absorbing plasma layer, and thus allow meaningful comparison with theoretical results.

Progress in this area requires close interactions between theory and experiment. Proper interpretation of experimental results is dependent on accurate theoretical models. It is, however, also evident that the present theoretical picture is not complete. In the current situation, ionization states may be computed from one model, equation of state from a second (or a combination of several), and conductivity from a third. The various models are not necessarily self-consistent. Yet in all cases the desired physical parameters such as ionization state, scattering cross sections, and thermodynamic functions, should stem from a common microscopic model. We believe that the next step in producing a clearer theoretical picture would be to provide all of the thermodynamic and transport data from a common theoretical framework describing the microscopic dynamics. Thus such a model would provide equation-of-state data, transport

properties, and ionization state (and perhaps a frequency-dependent conductivity) all self-consistently calculated from the same microscopic description. This self-consistent model could then be used as input data for hydrodynamic simulations as well as reflectivity and emission calculations for comparison with experiment results.

ACKNOWLEDGMENTS

We are grateful to R. M. More and Y. T. Lee for the use of their conductivity data and equation-of-state models, and to Los Alamos National Laboratory for providing the SESAME equation of state and the conductivity data of G. Rinker. This work is supported by the Natural Sciences and Engineering Research Council of Canada.

APPENDIX: MODIFIED BONDING CORRECTIONS IN QEOS

In this appendix we describe the modified bonding corrections we used to obtain a more realistic cohesive energy. This modification changes the density-temperature coordinates of the location of the critical point. The original Barnes correction uses a two-parameter expression [27,20]. The two parameters are determined by requiring that the bulk modulus at standard density match the experimental value, and that the total pressure is zero. The cohesive energy corresponds to the change in internal energy required to expand from standard density to infinite volume on the cold curve, i.e., $E_c = E(V \rightarrow \infty, T=0) - E(V_0, T=0)$, where V_0 is the specific volume at standard density. With no further parameters for adjustment the standard Barnes correction produces a cohesive energy that does not necessarily match the experimental result. For the region of expanded densities we replaced the Barners correction with a four-parameter empirical correction to account for chemical bonding and also produce the correct cohesive energy. (For compression $V < V_0$, the standard Barnes correction is still applied in our calculations.) The expression for the bonding pressure is

$$P_b(f) = 3K_b(1+2f)^{5/2}(a+f+\xi f^2+\zeta f^3) , \tag{A1}$$

where

$$f = \tfrac{1}{2}[(V_0/V)^{2/3}-1] . \tag{A2}$$

As with the Barnes correction, this expression is added to the other pressure contributions in the EOS to produce a total pressure. The parameter a takes on a negative value, hence the pressure correction describes a negative tension to cancel out the positive electron pressure produced by the Thomas-Fermi statistical model. This functional form is inspired by the Birch-Murnaghan equation of state which has been used successfully to fit the cold compression curves of many solids [47]. However, it should be noted that this expression is used in the present context in a purely empirical manner. The compression parameter f spans the interval $0 \geq f \geq -\frac{1}{2}$ as the volume ratio ranges from $1 \geq V_0/V \geq 0$. The correction to the internal energy (relative to standard conditions) corresponding to the bonding pressure in Eq. (A1) is

$$E_b(f) = -\int_{V_0}^{V} P_b dV = 9K_b V_0[af + \tfrac{1}{2}f^2 + \tfrac{1}{3}\xi f^3 + \tfrac{1}{4}\zeta f^4] . \tag{A3}$$

There are four free parameters in these expressions, K_b, a, ξ, and ζ, which are determined by four conditions. Three of these conditions arise directly from physical constraints, which are (i) the total pressure at normal solid density is zero; (ii) the bulk modulus at normal solid density matches the experimental values; (iii) the cohesive energy E_c matches the experimental value. These three constraints can be satisfied using Eq. (A1) truncated before the cubic term in f (i.e., $\zeta=0$). However, this approach leads to the unphysical result that the bonding pressure P_b becomes positive at some finite volume. This occurs because for $\zeta=0$ the polynomial in f passes through a zero somewhere in the interval $0 \leq f \leq -\frac{1}{2}$. Therefore we impose a fourth constraint which explicitly sets this polynomial to zero in the limit of infinite volume, i.e., $a+f+\xi f^2+\zeta f^3=0$ for $f=-\frac{1}{2}$. This gives the physically plausible result that $P_b \leq 0$ at all volumes $V \geq V_0$. From these four conditions it is easy to determine the coefficients in Eqs. (A1) and (A3).

$$K_b = K_{\mathrm{TF0}} - K_0 + \tfrac{5}{3}P_{\mathrm{TF0}} , \tag{A4}$$

$$a = -\frac{P_{\mathrm{TF0}}}{3K_b} , \tag{A5}$$

$$\xi = -2\left[\frac{16}{9}\frac{E_c + E_{\mathrm{TF0}}}{K_b V_0} - 3 - 18a\right] , \tag{A6}$$

$$\zeta = -4\left[\frac{16}{9}\frac{E_c + E_{\mathrm{TF0}}}{K_b V_0} + 2 + 20a\right] . \tag{A7}$$

The input constants required for evaluating these expressions are V_0, the bulk modulus at standard density K_0, and cohesive energy E_c. In addition the Thomas-Fermi electron pressure P_{TF0}, energy E_{TF0}, and bulk modulus K_{TF0} evaluated at zero temperature and standard density are required to complete the determination of the parameters.

[1] G. R. Gathers, J. W. Shaner, and R. L. Brier, Rev. Sci. Instrum. **47**, 471 (1976)

[2] G. R. Gathers, Int. J. Thermophys. **4**, 209 (1983); G. R. Gathers and Marvin Ross, J. Non-Cryst. Solids **61&62**, 59 (1984).

[3] V. L. Al'tshuler, A. V. Bushman, M. V. Zhernokletov, V. N. Zubarev, A. A. Leont'ev, and V. E. Fortov, Zh. Eksp. Teor. Fiz. **78**, 741 (1980) [Sov. Phys. JETP **51**, 373 (1980)].

[4] A. V. Bushman, B. L. Glushak, V. K. Gryaznov, M. V. Zhernokletov, I. K. Krasyuk, P. P. Pashinin, A. M. Prokhorov, V. Ya. Ternovoi, A. S. Filimonov, and V. E. Fortov, Pis'ma Zh. Eksp. Teor. Fiz. **44**, 481 (1986) [JETP Lett.

44, 619 (1986)].
[5] B. L. Glushak, A. P. Zharkov, M. V. Zhernokletov, V. Ya. Ternovoi, A. S. Filimonov, and V. E. Fortov, Zh. Eksp. Teor. Fiz. **96**, 1301 (1989) [Sov. Phys. JETP **69**, 739 (1989)].
[6] C. G. M. van Kessel and R. Sigel, Phys. Rev. Lett. **33**, 1020 (1974).
[7] L. Veeser and J. Solem, Phys. Rev. Lett. **40**, 1391 (1978).
[8] R. J. Trainor, J. W. Shaner, J. M. Auerbach, and N. C. Holmes, Phys. Rev. Lett. **42**, 1154 (1979).
[9] F. Cottet, J. P. Romain, R. Fabbro, and B. Faral, Phys. Rev. Lett. **52**, 1884 (1984).
[10] A. Ng, D. Parfeniuk, and L. DaSilva, Phys. Rev. Lett. **54**, 2604 (1985); Opt. Commun. **53**, 1389 (1984).
[11] A. Ng, D. Parfeniuk, L. DaSilva, P. Celliers, R. M. More, and Y. T. Lee, Phys. Rev. Lett. **57**, 1595 (1986); D. Parfeniuk, A. Ng, L. DaSilva, and P. Celliers, Opt. Commun. **56**, 425 (1985).
[12] H. M. Milchberg, R. R. Freeman, S. C. Davey, and R. M. More, Phys. Rev. Lett. **61**, 2364 (1988).
[13] G. A. Rinker, Phys. Rev. B **31**, 4207 (1985); **31**, 4220 (1985).
[14] A. Ng, D. Parfeniuk, P. Celliers, and L. DaSilva, *Shock Waves in Condensed Matter 1985 (Plenum, New York, 1986), p. 255.*
[15] L. DaSilva, A. Ng, and D. Parfeniuk, J. Appl. Phys. **58**, 3634 (1985).
[16] Ya. B. Zel'dovich and Yu. P. Raizer, Zh. Eksp. Teor. Fiz. **35**, 1402 (1958) [Sov. Phys. JETP **8**, 980 (1959)].
[17] Ya. B. Zel'dovich and Yu. P. Raizer, *The Physica of Shock Waves and High-Temperature Hydrodynamic Phenomena* (Academic, New York, 1966), p. 773.
[18] Y. T. Lee and R. M. More, Phys. Fluids **27**, 1273 (1984).
[19] K. S. Holian, Los Alamos National Laboratory Report No. LA-10160-MS UC-34, 1984 (unpublished).
[20] R. M. More, K. H. Warren, D. A. Young, and G. B. Zimmerman, Phys. Fluids **31**, 3059 (1988).
[21] K. Trainor, Lawrence Livermore National Laboratory Report No. UCID-18574-82-2, 1982 (unpublished).
[22] M. Ross, Phys. Rev. B **21**, 3140 (1980).
[23] F. J. Rogers, Phys. Rev. A **24**, 1531 (1981).
[24] C. A. Rouse, Astrophys. J. **134**, 435 (1961); **136**, 636 (1962).
[25] D. A. Young, Lawrence Livermore National Laboratory Report No. UCRL-52352, 1977 (unpublished).
[26] R. Latter, Phys. Rev. **99**, 510 (1955).
[27] John F. Barnes, Phys. Rev. **153**, 269 (1967).
[28] K. A. Gschneider, Jr., in *Solid State Physics: Advances in Research and Applications* (Academic, New York, 1964), Vol. 16, p. 275.
[29] L. E. Reichl, *A Modern Course in Statistical Physis* (University of Texas Press, Austin, 1980) p. 99.
[30] A. V. Grosse, J. Inorg. Nucl. Chem. **22**, 23 (1961).
[31] David A. Young and Berni J. Alder, Phys. Rev. A **3**, 364 (1971).
[32] V. E. Fortov, A. N. Dremin, and A. A. Leont'ev, High Temp. (USSR) **13**, 984 (1976) [Toplofiz. Vys. Temp. **13**, 1072 (1975)].
[33] J. Ziman, *Principles of the Theory of Solids,* 2nd ed. (Cambridge University Press, London, 1972), p. 221.
[34] R. Evans, B. L. Gyorffy, N. Szabo, and J. M. Ziman, in *The Properties of Liquid Metals,* edited by S. Takeuchi (Taylor & Francis, London, 1973), p. 319.
[35] D. A. Liberman, Comput. Phys. Commun. **2**, 107 (1971).
[36] D. A. Liberman, Phys. Rev. B **20**, 4981 (1979).
[37] W. A. Lokke and W. H. Grasberger, Lawrence Livermore National Laboratory Report No. UCRL-52276, 1977 (unpublished).
[38] D. Parfeniuk, A. Ng, and P. Celliers, Can. J. Phys. **66**, 662 (1988).
[39] H. M. Milchberg and R. R. Freeman, J. Opt. Soc. Am. B **6**, 1351 (1989).
[40] R. Fedosejevs, R. Ottman, R. Sigel, G. Kuhnle, S. Szatmari, and F. P. Shafer, Appl. Phys. B **50**, 79 (1990).
[41] Jean-Claude Kieffer, Jean-Pierre Matte, Stephane Belair, Mohamed Chaker, Patrick Audebert, Henri Pepin, P. Maine, D. Strickland, Philippe Bado, and Gerard Mourou, IEEE J. Quantum Electron. **25**, 2640 (1989).
[42] Max Born and Emil Wolf, *Principles of Optics,* 6th ed. (Pergamon, Oxford, 1980).
[43] T. E. Faber, *Introduction to the Theory of Liquid Metals* (Cambridge University Press, London, 1972), p. 385.
[44] John A. Moriarty, David A. Young, and Marvin Ross, Phys. Rev. B **30**, 578 (1984).
[45] V. L. Ginzburg, *Propagation of Electromagnetic Waves in Plasmas,* 2nd ed. (Pergamon, Oxford, 1970), p. 26.
[46] Ya. B. Zel'dovich and Yu. P. Raizer, Ref. [17], p. 271.
[47] F. Birch, J. Geophys. Res. **83**, 1257 (1978).